

# Development of a Lagrangian Particle Tracking Method for High-Order Discontinuous Galerkin Schemes

Eric Ching<sup>\*1</sup>, Steven Brill<sup>†2</sup>, Yu Lv<sup>‡3</sup>, and Matthias Ihme<sup>§1</sup>

<sup>1</sup>*Department of Mechanical Engineering, Stanford University,  
Stanford, CA 94305, United States*

<sup>2</sup>*Institute for Computational and Mathematical Engineering, Stanford University,  
Stanford, CA 94305, United States*

<sup>3</sup>*Department of Aerospace Engineering, Mississippi State University,  
Mississippi State, MS 39759, United States*

**This paper discusses the development of a Lagrangian particle method in a discontinuous Galerkin framework to support supersonic dusty flow simulations. This is relevant to reentry flows in the Mars atmosphere, which is characterized by the presence of a large number of suspended dust particles. These dust particles can not only enhance erosion of thermal protection systems but also transfer energy and momentum to the shock layer, increasing surface heat fluxes. This work represents a first step towards enabling high-fidelity simulations of high-speed flows in dusty environments using discontinuous Galerkin methods. Two-way coupling between the carrier and disperse phases is considered, and difficulties associated with searching for and locating particles in unstructured grids with curved elements are addressed. The particle method is applied to a number of test cases, including supersonic flows over a flat plate and a circular cylinder.**

## I. Introduction

Recent interest in human-scale missions to Mars has sparked active research into high-fidelity simulations of reentry flows. These complex aerothermodynamic environments are characterized by such physical phenomena as strong shocks, turbulence, dissociation, radiative heat transfer, and surface ablation. A key feature of the Mars atmosphere is the high levels of suspended dust particles, which can significantly influence the flow environment. During dust storms, suspended particles, on the order of microns in size, can reach altitudes up to 60 km [1], at which approximate flight velocities and Mach numbers are 7.4 km/s and 40, respectively, based on previous trajectory analyses [2].

Dust particles can interact with shocks, shock layers, and vehicle surfaces [3]. For instance, particles crossing a strong shock can induce shock perturbations that may affect downstream heat transfer. In addition, particles may experience break-up and phase changes, which can alter mass fluxes at the vehicle surface. In the post-shock region, particles and the surrounding flow exchange energy and momentum. In addition to experiencing slowdown and deflection, particles can undergo considerable heating, which can subsequently induce radiation to the vehicle surface. Furthermore, particles colliding with the vehicle surface can enhance erosion of thermal protection systems, and the resulting debris can interact with both particles and the flow. Finally, particle deposition can increase surface roughness, facilitating laminar-turbulent transition and increasing surface heat fluxes.

The complex physics prevalent in high-speed environments presents many challenges for flow simulations. Given the limitations of conventional numerical methods [4, 5], a promising alternative to commonly used second-order finite volume schemes is high-order discontinuous Galerkin (DG) methods [6]. Some notable advantages of DG schemes over classical methods include arbitrarily high spatial order of accuracy, geometric flexibility, a high degree of scalability, and the utilization of advanced *hp*-adaptation strategies. Having demonstrated success in areas such as aerodynamics [7], combustion [8], and turbulence [9], DG schemes have begun to show potential for the prediction of hypersonic flows [10, 11]. Particularly, in contrast with conventional finite-volume techniques, heating results computed with DG methods exhibit substantially lower sensitivities to grid topology and inviscid/viscous flux formulations.

---

\*eching@stanford.edu

†srbrill@stanford.edu

‡ylv@stanford.edu

§mihme@stanford.edu

Given the need to accurately assess the impact of dust particles on Mars re-entry vehicles, this work aims to develop a high-fidelity particle method for simulating particle-laden high-speed flow environments. To exploit the advantages of high-order numerical schemes, this method is formulated in a DG framework using a mesoscopic modeling approach. Development involves taking into account two-way coupling between the carrier and disperse phases as well as consideration of the challenges associated with searching for and locating particles in unstructured grids with curved elements. The particle method has been implemented in a high-order parallel DG solver capable of simulating viscous perfect-gas flows in the hypersonic regime [11]. The particle method described here has been applied to three test cases, two of which involve supersonic dusty flows, representing a first step towards high-fidelity simulations of hypersonic flows in dusty environments using DG schemes.

## II. Mathematical formulation

### A. Carrier phase governing equations

For describing the behavior of the carrier gas, the governing equations for conservation of mass, momentum, and total energy are written as

$$\partial_t \rho + \nabla \cdot (\rho \mathbf{u}) = 0, \quad (1a)$$

$$\partial_t (\rho \mathbf{u}) + \nabla \cdot (\rho \mathbf{u} \otimes \mathbf{u} + p \mathbf{I}) = \nabla \cdot \boldsymbol{\tau}, \quad (1b)$$

$$\partial_t (\rho E) + \nabla \cdot (\mathbf{u}(\rho E + p)) = \nabla \cdot (\mathbf{u} \cdot \boldsymbol{\tau} - \mathbf{q}), \quad (1c)$$

where the viscous stress tensor and heat flux are given as

$$\boldsymbol{\tau} = \mu[\nabla \mathbf{u} + (\nabla \mathbf{u})^T] - \frac{2}{3} \mu (\nabla \cdot \mathbf{u}) \mathbf{I}, \quad (2a)$$

$$\mathbf{q} = -\kappa \nabla T, \quad (2b)$$

respectively. In Eqs. (2),  $\mu$  is the dynamic viscosity, obtained using Sutherland's law for air,

$$\mu = \mu_{\text{ref}} \left( \frac{T}{T_{\text{ref}}} \right)^{1.5} \frac{T_{\text{ref}} + T_s}{T + T_s}, \quad (3)$$

where  $\mu_{\text{ref}}$  is the viscosity at the reference temperature  $T_{\text{ref}}$  and  $T_s$  is the Sutherland constant. In addition,  $\kappa = c_p \mu / \text{Pr}$  is the thermal conductivity, with  $\text{Pr}$  the Prandtl number and  $c_p = R\gamma / (\gamma - 1)$  the specific heat at constant pressure.  $R$  is the specific gas constant and  $\gamma$ , the specific heat ratio, is set to a value of 1.4 in this study. By the ideal gas law, pressure is related to internal energy as

$$p = (\gamma - 1) \left( \rho E - \frac{\rho}{2} |\mathbf{u}|^2 \right). \quad (4)$$

Equations (1) can be recast in vector form as

$$\partial_t \mathbf{U} + \nabla \cdot \mathbf{F}_{\mathbf{c}} = \nabla \cdot \mathbf{F}_{\mathbf{d}}, \quad (5)$$

where  $\mathbf{U}(\mathbf{x}, t) : \mathbb{R}^{N_d} \times \mathbb{R} \rightarrow \mathbb{R}^{N_U}$  is the conservative state vector,  $\mathbf{F}_{\mathbf{c}}(\mathbf{U}) : \mathbb{R}^{N_U} \rightarrow \mathbb{R}^{N_U \times N_d}$  is the convective flux vector, and  $\mathbf{F}_{\mathbf{d}}(\mathbf{U}, \nabla \mathbf{U}) : \mathbb{R}^{N_U} \times \mathbb{R}^{N_U \times N_d} \rightarrow \mathbb{R}^{N_U \times N_d}$  is the diffusive flux vector. In addition,  $\mathbf{x} \in \mathbb{R}^{N_d}$  is the spatial coordinate vector,  $t$  is the time,  $N_U$  is the number of state variables, and  $N_d$  is the number of spatial dimensions.

### B. Discontinuous Galerkin Discretization

To develop a discontinuous Galerkin framework, the problem is considered to be posed on the computational domain  $\Omega$  with boundary  $\partial\Omega$ .  $\Omega$  is partitioned into  $N_e$  non-overlapping discrete elements such that  $\Omega = \cup_{e=1}^{N_e} \Omega_e$ . The boundary of element  $\Omega_e$  is denoted by  $\partial\Omega_e$ . The global space of test functions is defined as

$$\mathcal{V} = \oplus_{e=1}^{N_e} \mathcal{V}_e, \quad \mathcal{V}_e = \text{span} \{ \phi_n(\Omega_e) \}_{n=1}^{N_b}, \quad (6)$$

with  $\phi_n$  the  $n$ th polynomial basis and  $N_b$  the number of basis functions. The global solution  $\mathbf{U}$  is approximated by  $\mathbf{U}$ , where

$$\mathbf{U} = \oplus_{e=1}^{N_e} \mathbf{U}^e, \quad \mathbf{U}^e \in \mathcal{V}_e. \quad (7)$$

The local solution approximation  $U^e$  is given by

$$\mathbf{U}^e(t, \mathbf{x}) = \sum_{m=1}^{N_b} \tilde{\mathbf{U}}_m^e(t) \phi_m(\mathbf{x}), \quad (8)$$

and the vector of basis coefficients  $\tilde{\mathbf{U}}^e(t) \in \mathbb{R}^{N_U \times N_b}$  is obtained from the discretized weak solution of

$$\sum_{m=1}^{N_b} d_t \tilde{\mathbf{U}}_m^e(t) \int_{\Omega_e} \phi_n \phi_m d\Omega_e + \int_{\Omega_e} \phi_n \nabla \cdot \mathbf{F}_c d\Omega_e = \int_{\Omega_e} \phi_n \nabla \cdot \mathbf{F}_d d\Omega_e, \quad (9)$$

$\forall \phi_n$ , where  $n = 1, \dots, N_b$ .  $\mathbf{F}_c$  and  $\mathbf{F}_d$  are the approximations to  $\mathbf{F}_c$  and  $\mathbf{F}_d$ , respectively.

To solve the variational formulation in Eq. (9), integration by parts is performed on the convective and viscous terms, resulting in the emergence of surface integrals through which boundary and interface conditions are weakly imposed. In this study, the Roe inviscid flux function [12] and the BR2 scheme [13] are employed to define the convective flux and viscous flux contributions, respectively. In addition, to capture shocks, pressure jumps are used for shock detection while smooth artificial viscosity is used for stabilization. Further details can be found in Ref. [11].

### C. Disperse phase governing equations

Lagrangian particle tracking is used to compute the behavior of the disperse phase in the flow field. To simplify the calculations, individual particles are treated as smooth, solid, non-rotating, inert spheres with fixed diameters that exchange only momentum and energy with the carrier phase. It is assumed that particles do not interact with each other, and their motion is driven by drag only. The particle temperature is assumed to be uniform over the entire particle. In addition, the disperse phase is considered to be dilute, such that the particle volume fraction is neglected. The particle state is computed using the following set of ordinary differential equations:

$$\frac{d\mathbf{x}_d}{dt} = \mathbf{u}_d, \quad (10a)$$

$$m_d \frac{d\mathbf{u}_d}{dt} = \mathbf{F}, \quad (10b)$$

$$m_d c_d \frac{dT_d}{dt} = Q, \quad (10c)$$

where, representing the carrier and disperse phases using the ‘‘c’’ and ‘‘d’’ subscripts, respectively,  $\mathbf{x}_d$  is the particle position,  $\mathbf{u}_d$  is the particle velocity,  $m_d = \rho_d \frac{\pi}{6} D_d^3$  is the particle mass (with  $\rho_d$  the particle density and  $D_d$  the particle diameter),  $c_d$  is the specific heat of the particle, and  $T_d$  is the particle temperature. The drag force  $\mathbf{F}$  and the heating rate  $Q$  take the following form:

$$\mathbf{F} = \frac{1}{8} \pi D_d^2 \rho_c (\mathbf{u}_c - \mathbf{u}_d) |\mathbf{u}_c - \mathbf{u}_d| C_D, \quad (11a)$$

$$Q = \pi D_d \kappa_c (T_c - T_d) \text{Nu}, \quad (11b)$$

In this work, two different correlations for computing the drag coefficient  $C_D$  are employed. The first is simple Stokes drag, which calculates the drag coefficient as  $C_D = 24/\text{Re}_p$ , where  $\text{Re}_p = \rho_c |\mathbf{u}_c - \mathbf{u}_d| D_d / \mu_c$  is the relative particle Reynolds number. The second is Henderson’s correlations [14], which compute  $C_D$  as a function of  $\text{Re}_p$ , the relative particle Mach number  $\text{Ma}_p = |\mathbf{u}_c - \mathbf{u}_d| / (\gamma p_c / \rho_c)^{0.5}$ , and the temperature ratio  $T_d/T_c$ . Furthermore, the Nusselt number  $\text{Nu}$  is calculated either from the creeping flow limit, where  $\text{Nu} = 2$ , or from the formula proposed by Fox *et al.* [15], given as

$$\text{Nu} = \frac{2 \exp(-\text{Ma}_p)}{1 + 17 \frac{\text{Ma}_p}{\text{Re}_p}} + 0.459 \text{Pr}^{0.33} \text{Re}_p^{0.55} \frac{1 + 0.5 \exp(-17 \frac{\text{Ma}_p}{\text{Re}_p})}{1.5}. \quad (12)$$

Note that the Stokes drag correlation and the creeping flow limit value for the Nusselt number are used in this study only for verification purposes. They are not typically representative of realistic conditions.

In calculating  $\mathbf{F}$  and  $Q$  in Eqs. (11), to preserve accuracy, the carrier phase state is evaluated at the particle position  $\mathbf{x}_d$  with the same basis functions used to construct the local solution approximation, i.e.  $\mathbf{U}^e(t, \mathbf{x}_d) = \sum_{m=1}^{N_b} \tilde{\mathbf{U}}_m^e(t) \phi_m(\mathbf{x}_d)$ .

#### D. Two-way coupling methodology

To translate the effect of the particles on the flow field, the following source term is added to the RHS of Eq. (5):

$$\mathbf{S} = [0, \langle \mathbf{F} \rangle, \langle Q \rangle + \langle W \rangle]^T, \quad (13)$$

where

$$\langle \mathbf{F} \rangle = \sum_{i=1}^{N_p} \mathbf{F}_i \psi(\mathbf{x} - \mathbf{x}_{d,i}), \quad (14a)$$

$$\langle Q \rangle = \sum_{i=1}^{N_p} Q_i \psi(\mathbf{x} - \mathbf{x}_{d,i}), \quad (14b)$$

$$\langle W \rangle = \sum_{i=1}^{N_p} \mathbf{u}_{d,i} \cdot \mathbf{F}_i \psi(\mathbf{x} - \mathbf{x}_{d,i}), \quad (14c)$$

where  $W$  is the work done by particle drag and  $N_p$  is the total number of particles in the entire domain.  $\psi(\mathbf{x} - \mathbf{x}_{d,i})$  is a particle shape function that weighs the particle influence to the flow field and satisfies the property  $\int_{\Omega} \psi d\Omega = 1$ . In this work,  $\psi(\mathbf{x} - \mathbf{x}_{d,i}) = \delta(\mathbf{x} - \mathbf{x}_{d,i})$ , the Dirac delta function. Using this choice of shape function, the source term in the resulting variational formulation can be evaluated for  $\Omega_e$  analytically as

$$\int_{\Omega_e} \phi_n \mathbf{S} d\Omega_e = \sum_{i=1}^{N_p^e} \phi_n(\mathbf{x}_{d,i}) [0, \mathbf{F}_i, Q_i + \mathbf{u}_{d,i} \cdot \mathbf{F}_i]^T, \quad (15)$$

where  $N_p^e$  is the number of particles located in element  $\Omega_e$ . Investigating the use of smoother shape functions, such as truncated cosine, Gaussian, and polynomial functions, will be the subject of future work [16].

In this study, the disperse and carrier phases are loosely coupled in a similar manner as in Ref. [17]. The time step of the disperse phase is computed such that it is no greater than the carrier phase time step, particles do not cross more than one element, and the particle velocity  $\mathbf{u}_d$  monotonically approaches the carrier gas velocity  $\mathbf{u}_c$ . Within each carrier phase time step, the two phases are evolved in time independently of each other.

#### E. Particle search algorithm

As discussed previously, the carrier phase state must be interpolated at the particle position in solving Eqs. (10). This involves not only identifying the host element of each particle but also mapping the physical position of the particle,  $\mathbf{x}_d$ , to the reference position associated with the parent element,  $\xi_d$ . For DG schemes, in which unstructured grids consisting of curved elements are often used, this presents major challenges. The algorithm presented by Allievi and Bermejo [18] is thus employed for particle localization, summarized here for 2D quadrilaterals of quadratic order.

Let  $\hat{\Omega}$  denote the reference quadrilateral such that

$$\hat{\Omega} = \{(\xi, \eta) | -1 \leq \xi, \eta \leq 1\}. \quad (16)$$

Then, letting  $\xi = (\xi, \eta)$ , the isoparametric mapping  $F_e : \hat{\Omega} \rightarrow \Omega_e$  is given as

$$F_{1e}(\xi) \equiv x = \sum_{i=1}^{N_n} \Phi_i(\xi) x_i^e, \quad (17a)$$

$$F_{2e}(\xi) \equiv y = \sum_{i=1}^{N_n} \Phi_i(\xi) y_i^e, \quad (17b)$$

where  $(x_i^e, y_i^e)_{i=1}^{N_n}$  denotes the physical coordinates of the  $N_n$  geometric nodes of  $\Omega_e$  and  $\{\Phi_i\}_{i=1}^{N_n}$  are the basis functions for geometry interpolation. This is illustrated schematically in Figure 1. With a standard Lagrangian basis, the

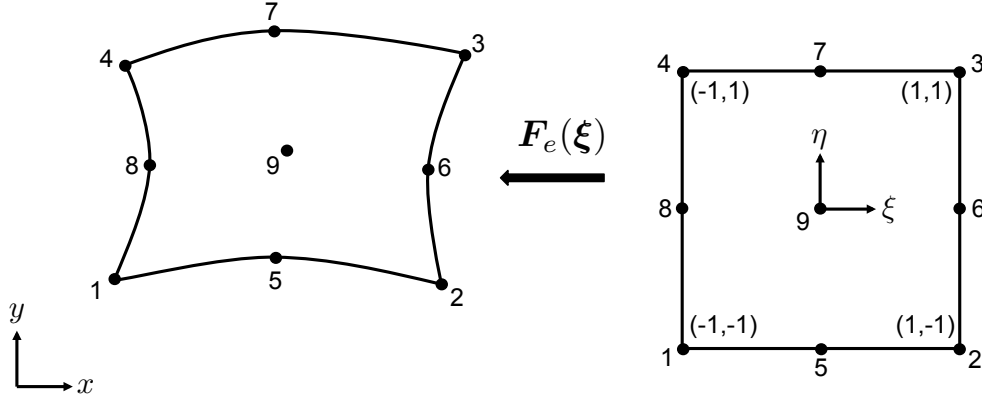


**Fig. 1 Isoparametric mapping for quadrilateral elements of quadratic order.**

basis functions for a reference quadrilateral of quadratic order are given by

$$\Phi_1(\xi) = \frac{1}{4}\xi\eta(1-\xi)(1-\eta), \quad (18a)$$

$$\Phi_2(\xi) = \frac{1}{4}\xi\eta(1+\xi)(\eta-1), \quad (18b)$$

$$\Phi_3(\xi) = \frac{1}{4}\xi\eta(1+\xi)(1+\eta), \quad (18c)$$

$$\Phi_4(\xi) = \frac{1}{4}\xi\eta(\xi-1)(1+\eta), \quad (18d)$$

$$\Phi_5(\xi) = \frac{1}{4}\eta(1-\xi^2)(\eta-1), \quad (18e)$$

$$\Phi_6(\xi) = \frac{1}{2}\xi(1+\xi)(1-\eta^2), \quad (18f)$$

$$\Phi_7(\xi) = \frac{1}{2}\eta(1-\xi^2)(\eta+1), \quad (18g)$$

$$\Phi_8(\xi) = \frac{1}{2}\xi(\xi-1)(1-\eta^2), \quad (18h)$$

$$\Phi_9(\xi) = (1-\xi^2)(1-\eta^2). \quad (18i)$$

If a point  $\mathbf{x}_d = (x_d, y_d) \in \Omega$  is in  $\Omega_e$ , then there exists  $\xi_d = (\xi_d, \eta_d) \in \hat{\Omega}$  such that

$$\mathbf{G}_e(\xi_d) \equiv \mathbf{x}_d - \mathbf{F}_e(\xi_d) = 0. \quad (19)$$

Note that in general, solving Eq. (19) for  $\xi_d$  cannot be done analytically. As such, Newton's method is employed in the following fashion: letting  $\xi^1 \in \hat{\Omega}$  be an initial guess, for  $k = 1, \dots, N_k$ ,

$$\xi^{k+1} = \xi^k - \mathbf{J}_e^{-1}(\xi^k)\mathbf{G}_e(\xi^k), \quad (20)$$

where  $N_k$  is the number of Newton iterations until either convergence or another stopping criterion is reached and  $\mathbf{J}_e^{-1}(\xi)$  is the inverse of the Jacobian matrix of the mapping  $\mathbf{F}_e$ . If convergence is attained and  $\xi^{N_k+1} \in \hat{\Omega}$  according to Eq. (16), then the host element has been identified and  $\xi_d = \xi^{N_k+1}$ . However, if  $\xi^{N_k+1} \notin \hat{\Omega}$ , then another element must be searched. The selection of the next element to check is important since the computational cost can increase drastically if a large number of elements are unnecessarily checked. In the algorithm of Allievi and Bermejo [18], one of the eight vertex-sharing elements is selected based on the values of  $(\xi^{N_k+1}, \eta^{N_k+1})$ , shown schematically in Figure 2. This results in a fairly efficient methodology for identifying the host element of a particle and calculating the reference position. In the context of particle tracking, the particle search algorithm at each time step can be summarized as follows for a particle located at physical position  $\mathbf{x}_d$ :

- 1) Perform Newton's method on the host element from the previous time step.

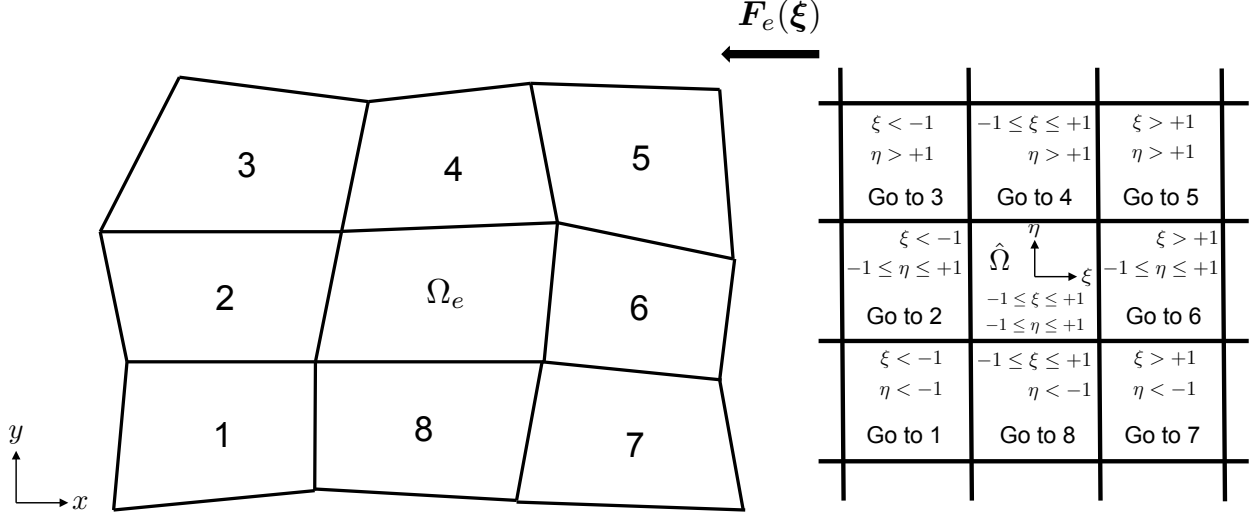


**Fig. 2** Instructions for selecting next element to search based on values of reference position  $\xi = (\xi, \eta)$ .

- 2) If  $\xi^{N_k+1}$  is inside the element according to Eq. (16), then the host element has been identified and  $\xi_d = \xi^{N_k+1}$ . If not, go to the next step.
- 3) Select new element to search based on Figure 2.
- 4) Perform Newton's method on selected element. Go back to Step 2.

This algorithm can be readily extended to higher orders and to 3D hexahedra. Further details are provided in Ref. [18] for triangular elements.

### III. Numerical examples

This section presents results for a number of test cases obtained using the Lagrangian particle method. The first test case is a sphere settling in a quiescent fluid at low Reynolds number. The second test case consists of supersonic dusty flow over a flat plate, and the final test case is supersonic dusty flow over a circular cylinder. Theoretical results are provided for comparison for the first two configurations.

#### A. Particle settling in a quiescent fluid

This numerical test is performed to ascertain whether the particle solver can correctly produce the temporal evolution of velocity of a particle initially at rest settling in a stationary fluid under the influence of gravity. The effects of the particle on the carrier phase are not taken into account. The external force on the particle is modified to include the gravitational body force as

$$\mathbf{F} = \frac{1}{8}\pi D_d^2 \rho_c (\mathbf{u}_c - \mathbf{u}_d) |\mathbf{u}_c - \mathbf{u}_d| C_D + (\rho_d - \rho_c) \frac{\pi}{6} D_d^3 \mathbf{g}, \quad (21)$$

where  $\mathbf{g}$  is the gravitational acceleration. Using the Stokes drag correlation to compute  $C_D$ , which is valid in the low Reynolds number limit, the theoretically predicted expression for particle velocity is given by

$$\mathbf{u}_d(t) = U \frac{\mathbf{g}}{|\mathbf{g}|} \left[ 1 - \exp\left(-\frac{t}{\tau_d}\right) \right], \quad U = \tau_d |\mathbf{g}| \frac{\rho_d - \rho_c}{\rho_d}, \quad (22)$$

where  $\tau_d = \rho_d D_d^2 / (18\mu_c)$  is the particle momentum relaxation time. At steady state when the particle drag force is balanced by the gravitational force, the particle speed is equal to  $U$ .

Two solutions were computed on a  $16^3$  hexahedral mesh in a periodic domain with polynomial order  $p = 2$  for the solution approximation. The particle Reynolds number is  $\text{Re}_p = 0.001$ . The first solution was calculated using Stokes drag, and the second solution was obtained using Henderson's correlations, which should recover Stokes drag at small Reynolds numbers. The time step was small enough such that temporal discretization errors were negligible. Figure

3 shows the temporal evolution of velocity for the two solutions compared with theoretical results. The Stokes drag numerical results agree very well with the theoretical results. Furthermore, only very slight discrepancies exist between the Henderson drag numerical results and the Stokes drag results, as expected at such a low Reynolds number.

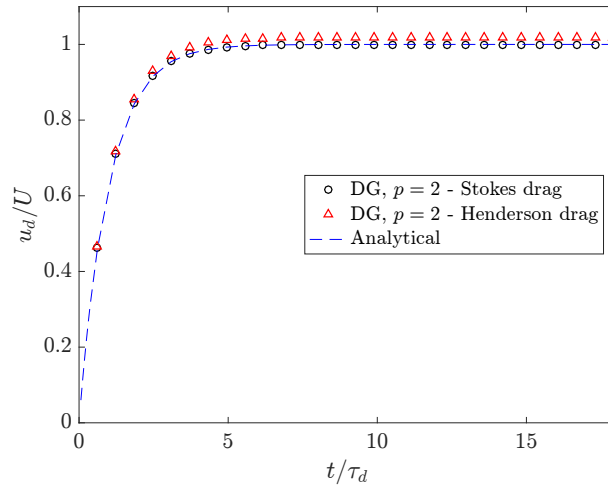


**Fig. 3** Temporal evolution of particle velocity for a particle settling in a quiescent fluid with  $Re_p = 0.001$ . Results are presented from theory and two DG solutions with different drag correlations.

### B. Supersonic dusty flow over a flat plate

Previously, Wang and Glass analytically investigated steady compressible laminar boundary-layer flows of a dilute dusty gas over a semi-infinite flat plate [19]. As shown in Figure 4, the dusty gas flow field can be divided into three distinct regions: the large-slip region near the leading edge (I), the moderate-slip region (II), and the small-slip region far downstream (III). Wang and Glass used a series-expansion method to compute the asymptotic solutions for the large-slip and small-slip regions. Numerical results are presented here for the large-slip region.

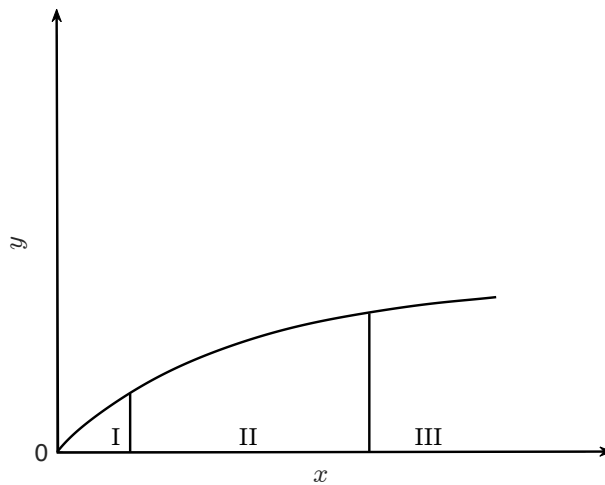


**Fig. 4** Schematic of compressible dusty gas over a flat plate showing three distinct regions: the large-slip region I, the moderate-slip region II, and the small-slip region III.

The flow parameters used for this test case are described in Table 1. The characteristic length scale is the momentum relaxation length  $\lambda_d = \tau_d u_\infty$  of the monodisperse particle phase, where  $u_\infty$  is the freestream velocity magnitude. Inflow boundary conditions are specified based on freestream parameters, extrapolation is used for the outflow boundary

conditions, and the surface of the plate is prescribed by an isothermal non-slip wall.

$Ma_\infty$	$Re_\infty$	$T_w/T_\infty$	$T_s(K)$	$\beta$	Pr	$D_d$ (m)	$\rho_d$ (kg/m <sup>3</sup> )
1.5	$10^4$	0.5	0.0	1.0	1.0	10E-06	2700

**Table 1** Flow parameters for supersonic dusty flow over a flat plate.  $Ma_\infty$  is the freestream Mach number,  $Re_\infty$  is the freestream Reynolds number,  $T_w$  is the cylinder wall temperature,  $T_\infty$  is the free-stream temperature, and  $\beta$  is the mass loading ratio between the disperse and carrier phases.  $Re_\infty$  is based on the particle momentum relaxation length,  $\lambda_d$ .

The simulation was performed with  $p = 2$  on a 2D quadrilateral mesh with 56 elements in the streamwise direction and 80 elements in the wall-normal direction. The mesh was refined near the wall and the leading edge of the flat plate. The carrier phase was integrated in time using implicit third-order backward differencing whereas the disperse phase was evolved with a third-order explicit Adams-Bashforth method. At each time step, particles were injected at freestream conditions at random locations along the leftmost inflow boundary based on the mass loading ratio  $\beta = 1$ . The simulation was run until quasi-steady-state conditions were reached. For consistency with the theoretical results, Stokes drag was used to compute the drag coefficient, and the Nusselt number follows the creeping flow limit value,  $Nu = 2$ .

In Figure 5, where  $(\cdot)^*$  corresponds to nondimensionalized quantities, the computed velocity and temperature profiles are compared with results from theory at  $x^* = 0.1$ . Outside the boundary layer, there are slight discrepancies as a result of a weak compression wave that emerges likely due to the prescription of freestream conditions at the inflow boundary instead of the analytical solution. Despite these leading edge effects, very good agreement is observed in the boundary layer, illustrating the capabilities of the two-way-coupling methodology to accurately predict boundary-layer quantities.

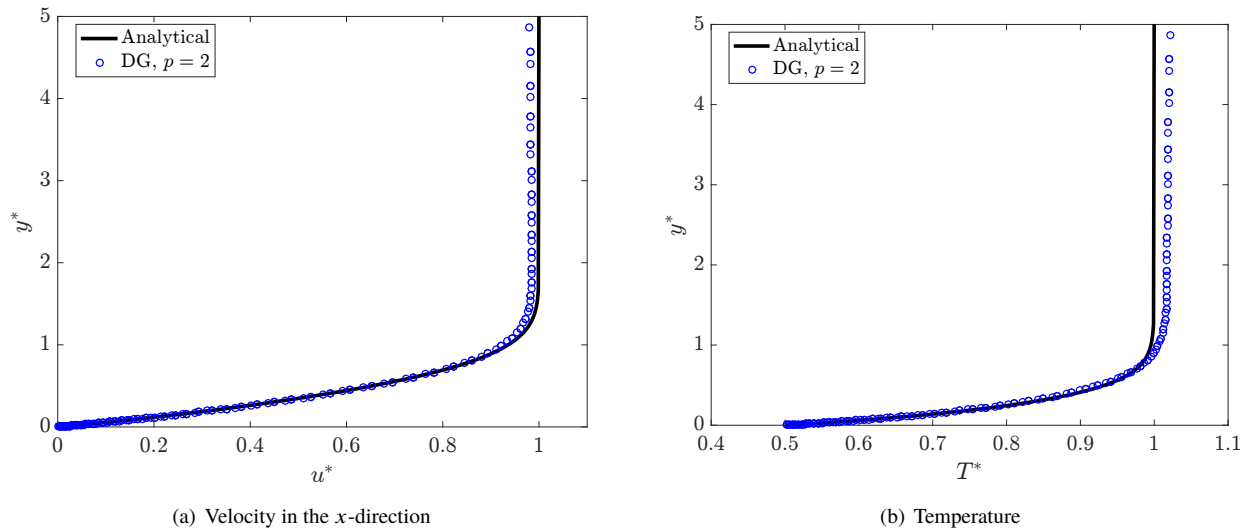


**Fig. 5** Nondimensionalized velocity and temperature profiles of the carrier phase at  $x^* = 0.1$  for supersonic dusty flow over a flat plate. Numerical and theoretical results are presented.

The nondimensionalized heat flux along the entire flat plate in the computational domain is displayed in Figure 6 for the theoretical and numerical results for both the pure and dusty gases. Slight heating augmentation is observed in the dusty gas results due to the transfer of kinetic and thermal energy from the disperse phase to the carrier phase. In each of the pure and dusty gas cases, there is very good agreement between the numerical and theoretical solutions. Slightly greater discrepancies are observed at larger  $x^*$  since the large-slip assumption begins to break down.

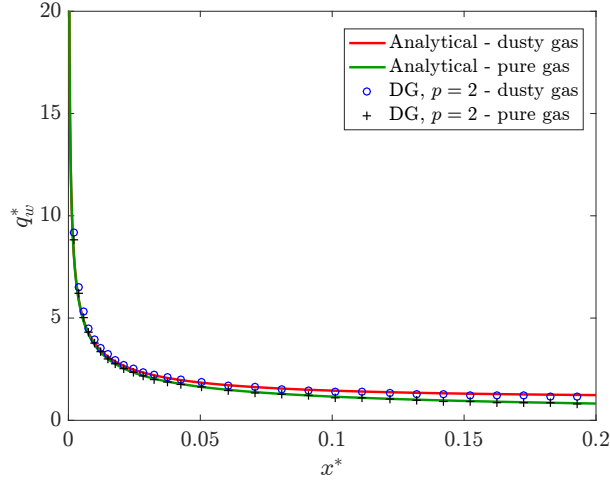


**Fig. 6 Nondimensionalized heat flux along the flat plate for both the pure and dusty gases. Theoretical and numerical results are provided.**

### C. Supersonic flow over a circular cylinder

The flow parameters for the configuration investigated in this section are listed in Table 2. Inflow boundary conditions are specified and extrapolation is used for the outflow boundary conditions. The surface of the cylinder, with diameter  $D$ , is prescribed by an isothermal no-slip wall.

$Ma_\infty$	$Re_\infty$	$T_w/T_\infty$	$T_s(K)$	$\beta$	Pr	$\rho_d$ (kg/m <sup>3</sup> )
2.0	$10^3$	1.0	110.4	0.15	0.71	2500

**Table 2 Flow parameters for supersonic dusty flow over a circular cylinder.  $Ma_\infty$  is the freestream Mach number,  $Re_\infty$  is the freestream Reynolds number,  $T_w$  is the cylinder wall temperature,  $T_\infty$  is the free-stream temperature, and  $\beta$  is the mass loading ratio between the disperse and carrier phases.  $Re_\infty$  is based on the cylinder diameter.**

The solution was computed with  $p = 3$  on a 2D quadrilateral mesh with 20 elements each in the wall-normal and circumferential directions. The mesh was refined in the wall-normal direction. The carrier phase was integrated in time using an explicit fourth-order Runge-Kutta method, while an explicit fourth-order Adams-Bashforth scheme was used to integrate the disperse phase. After reaching a steady-state pure-gas solution, particles were injected at freestream conditions at random positions along a narrow centered portion of the inflow boundary. In this test case, particles hitting the cylinder wall are reflected without loss of kinetic or thermal energy, and the cylinder wall was analytically prescribed. Ongoing work involves computing particle-wall collisions for general boundaries and accounting for energy transfer due to such collisions. The simulation was run for approximately eight flow-through times ( $t^* \equiv t/t_{\text{ref}} = 8$ , with  $t_{\text{ref}} = D/u_\infty$ ); additional simulation time would not significantly change quantities of interest.

Two particle momentum Stokes numbers, given by  $St = \tau_d/\tau_{\text{ref}}$ , were considered: 0.1 and 1. Figure 7 displays the locations of the  $St = 0.1$  particles and the  $St = 1$  particles at the end of the simulation. Compared to the  $St = 0.1$  particles, the  $St = 1$  particles are more resistant to the carrier flow, hit the wall more frequently, and form a large accumulation zone near the cylinder due to collisions with the wall and influence by the carrier gas.

The wall heat flux profiles for the two dusty-gas solutions are displayed in Figure 8. Adding particles to the flow increases the surface heat flux. Particles are heated up by the flow in the post-shock region and then transfer energy to the boundary layer, which in turn increases the head load to the cylinder. Near the stagnation point, the  $St = 0.1$  particles yield greater heat flux augmentation than the  $St = 1$  particles. However, farther from the stagnation point, the opposite is true. This is likely due to the relative dearth of  $St = 0.1$  particles in the boundary layer in this region compared to the  $St = 1$  particles, as illustrated in Figure 7. Accounting for inelastic particle-wall collisions and the consequent energy transfer would likely amplify the extent of heating augmentation, particularly for the higher Stokes numbers.

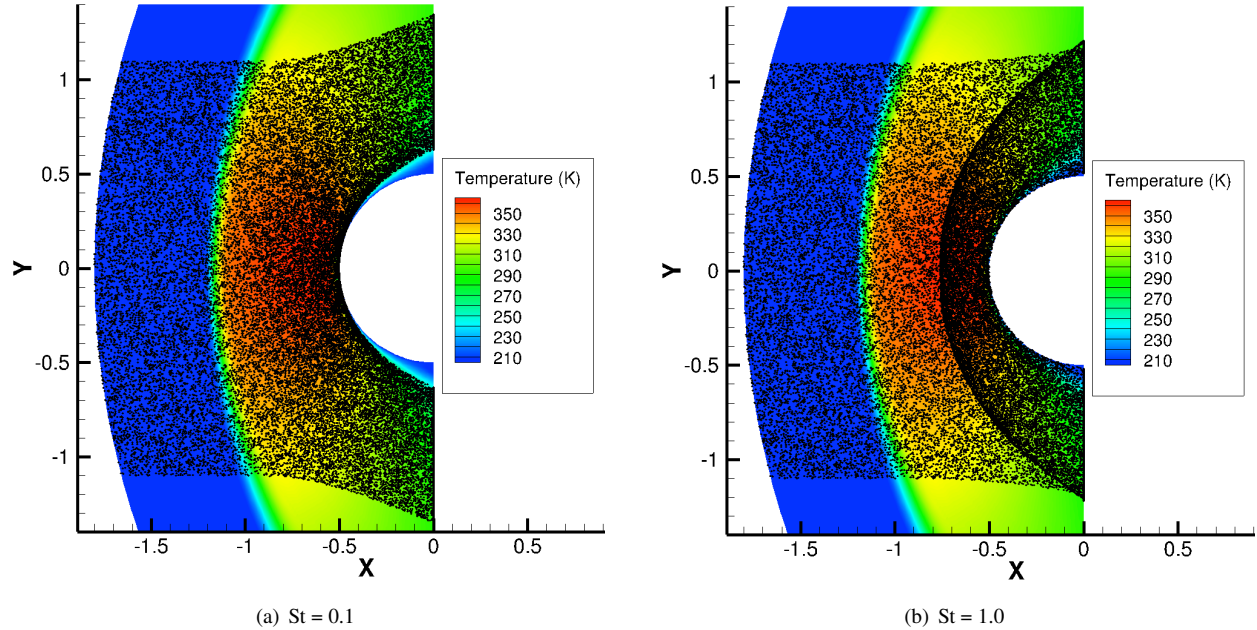


**Fig. 7** Locations of particles of different Stokes numbers at eight flow-through times, superimposed on the pure-gas temperature field, for Mach 2 flow over a circular cylinder. For the  $St = 0.1$  particles, approximately 3% of the total number of particles are shown. Particles were continuously injected at freestream conditions at random positions along a narrow curve along the inflow boundary.

#### IV. Summary and Ongoing Work

A Lagrangian point-particle method was developed in a high-order discontinuous Galerkin framework. Momentum and energy exchange between the carrier and disperse phases is accounted for. The formulas for particle drag force and heating rate depend on the relative particle Mach and Reynolds numbers. Delta functions are used for weighing the particle influence to the flow field. To locate the host element of a particle and map global position to reference position, the algorithm presented by Allievi and Bermejo [18] is employed. The particle method has been applied to three test cases: a particle settling in a quiescent fluid at low Reynolds number, supersonic dusty flow over a flat plate, and supersonic dusty flow over a circular cylinder. For the first two test cases, good agreement with theoretical predictions is observed. In the third test case, appreciable heating augmentation is observed for monodisperse dusty flows with Stokes numbers of 0.1 and 1. Ongoing work entails implementing more sophisticated boundary conditions and applying the particle method to additional test cases, such as hypersonic dusty flows over blunt bodies to assess particle-induced heating augmentation. Smoother particle shape functions may also be considered.

#### Acknowledgments

This work was supported by a Stanford Graduate Fellowship and an Early Career Faculty grant from NASA's Space Technology Research Grants Program. Discussions with Michael Barnhardt of NASA Ames and Peter Gnoffo of NASA Langley are greatly appreciated.

#### References

- [1] Papadopoulos, P. E., "Computation of heat shield erosion in a dusty Martian atmosphere," Stanford University Ph.D. Thesis, 1994.
- [2] Subrahmanyam, P., "Discontinuous Galerkin methods for computational aerodynamics – 3D adaptive flow simulation with the DLR PADGE code," *International Journal of Aerospace Engineering*, Vol. 14, No. 7, 2010, pp. 512–519.
- [3] Montois, I., Pirottais, D., Conte, D., Sauvage, N., and Chazot, O., "Overview of dust effects during Mars atmospheric entries: models, facilities, and design tools," Tech. rep.

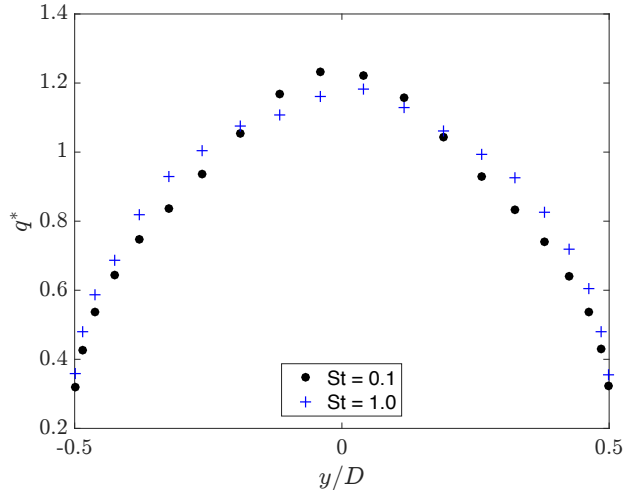


**Fig. 8 Comparison of nondimensionalized cylinder wall heat flux profiles for the two dusty-flow solutions.  $q^*$  is the dusty-gas heat flux normalized by the pure-gas stagnation-point heat flux.**

- [4] Gnoffo, P. A., and White, J. A., “Computational aerothermodynamic simulation issues on unstructured grids,” *37th AIAA Thermophysics Conference*, AIAA 2004-2371, Portland, Oregon, 2004.
- [5] Kitamura, K., Shima, E., Nakamura, Y., and Roe, P. L., “Evaluation of Euler fluxes for hypersonic heating computations,” *AIAA Journal*, Vol. 48, No. 4, 2010, pp. 763–776.
- [6] Wang, Z., Fidkowski, K., Abgrall, R., Bassi, F., Caraeni, D., Cary, A., Deconinck, H., Hartmann, R., Hillewaert, K., Huynh, H., Kroll, N., May, G., Persson, P.-O., van Leer, B., and Visbal, M., “High-order CFD methods: current status and perspective,” *International Journal for Numerical Methods in Fluids*, Vol. 72, 2013, pp. 811–845.
- [7] Hartmann, R., Held, J., Leicht, T., and Prill, F., “Discontinuous Galerkin methods for computational aerodynamics – 3D adaptive flow simulation with the DLR PADGE code,” *Aerospace Science and Technology*, Vol. 14, No. 7, 2010, pp. 512–519.
- [8] Lv, Y., and Ihme, M., “Discontinuous Galerkin method for multicomponent chemically reacting flows and combustion,” *Journal of Computational Physics*, Vol. 270, 2014, pp. 105–137.
- [9] Lv, Y., Ma, P. C., and Ihme, M., “On underresolved simulations of compressible turbulence using an entropy-bounded DG method: solution stabilization, scheme optimization, and benchmark against a finite-volume solver,” *Computers & Fluids*, 2017. doi:10.1016/j.compfluid.2017.11.016.
- [10] Barter, G. E., and Darmofal, D. L., “Shock capturing with PDE-based artificial viscosity for DGFEM: Part I. Formulation,” *Journal of Computational Physics*, Vol. 229, No. 5, 2010, pp. 1810–1827.
- [11] Ching, E. J., Lv, Y., and Ihme, M., “Development of discontinuous Galerkin method for hypersonic heating prediction,” *55th AIAA Aerospace Sciences Meeting*, AIAA 2017-0311, Grapevine, Texas, 2017.
- [12] Roe, P. L., “Approximate Riemann solvers, parameter vectors, and difference schemes,” *Journal of Computational Physics*, Vol. 43, No. 2, 1981, pp. 357–372.
- [13] Bassi, F., and Rebay, S., “GMRES discontinuous Galerkin solution of the compressible Navier-Stokes equations,” *Discontinuous Galerkin Methods: Theory, Computation and Applications*, edited by B. Cockburn and C.-W. Shu, Springer, Berlin, 2000, pp. 197–208.
- [14] Henderson, C. B., “Drag coefficients of spheres in continuum and rarefied flows,” *AIAA J*, Vol. 14, No. 6, 1976, pp. 707–708.
- [15] Fox, T. W., Rackett, C. W., and Nicholls, J. A., “Shock wave ignition of magnesium powders,” *11th International Shock Tubes and Waves Symposium*, Seattle, Washington, 1978, pp. 262–268.
- [16] Jacobs, G., and Hesthaven, J. S., “High-order nodal discontinuous Galerkin particle-in-cell method on unstructured grids,” *Journal of Computational Physics*, Vol. 214, 2006, pp. 96–121.

- [17] Majid, A., and Fertig, M., “Two-phase flow solver for hypersonic entry flows in a dusty Martian atmosphere,” *Journal of Thermophysics and Heat Transfer*, Vol. 30, No. 2, 2016.
- [18] Allievi, A., and Bermejo, R., “A generalized particle search-locate algorithm for arbitrary grids,” *Journal of Computational Physics*, Vol. 132, 1997, pp. 157–166.
- [19] Wang, B. Y., and Glass, I. I., “Compressible laminar boundary-layer flows of a dusty gas over a semi-infinite flat plate,” *Journal of Fluid Mechanics*, Vol. 186, 1988, pp. 223–241.